Structural Basis for Tumor Pyruvate Kinase M2 Allosteric Regulation and Catalysis[†,‡]

Jill D. Dombrauckas, Bernard D. Santarsiero, and Andrew D. Mesecar*

Center for Pharmaceutical Biotechnology and Department of Medicinal Chemistry and Pharmacognosy, University of Illinois at Chicago, Chicago, Illinois 60607

Received November 29, 2004; Revised Manuscript Received May 13, 2005

ABSTRACT: Four isozymes of pyruvate kinase are differentially expressed in human tissue. Human pyruvate kinase isozyme M2 (hPKM2) is expressed in early fetal tissues and is progressively replaced by the other three isozymes, M1, R, and L, immediately after birth. In most cancer cells, hPKM2 is once again expressed to promote tumor cell proliferation. Because of its almost ubiquitous presence in cancer cells, hPKM2 has been designated as tumor specific PK-M2, and its presence in human plasma is currently being used as a molecular marker for the diagnosis of various cancers. The X-ray structure of human hPKM2 complexed with Mg^{2+}, K^+, the inhibitor oxalate, and the allosteric activator fructose 1,6-bisphosphate (FBP) has been determined to a resolution of 2.82 Å. The active site of hPKM2 is in a partially closed conformation most likely resulting from a ligand-induced domain closure promoted by the binding of FBP. In all four subunits of the enzyme tetramer, a conserved water molecule is observed on the 2-*si* face of the prospective enolate and supports the hypothesis that a proton-relay system is acting as the proton donor of the reaction (*1*). Significant structural differences among the human M2, rabbit muscle M1, and the human R isozymes are observed, especially in the orientation of the FBP-activating loop, which is in a closed conformation when FBP is bound. The structural differences observed between the PK isozymes could potentially be exploited as unique structural templates for the design of allosteric drugs against the disease states associated with the various PK isozymes, especially cancer and nonspherocytic hemolytic anemia.

Tumor cells utilize an excess of energy in order to proliferate, and they require an abundance of essential nutrients, such as glucose, in order to synthesize components for cellular replication (*2*). The delicate balance necessary to achieve both of these goals, while enduring unfavorable conditions typical for tumor cells such as hypoxia and low glucose supply, is complex. Pyruvate kinase (PK)[1] is an important regulatory enzyme that is able to generate ATP under hypoxic conditions as well as regulate glucose consumption. Pyruvate kinase catalyzes the last step in glycolysis converting the substrate phosphoenolpyruvate (PEP) into pyruvate, while producing one molecule of ATP per reaction per cycle (Figure 1A). The forward reaction and generation of ATP are strongly favored because PEP releases a significant amount of energy in comparison to ATP ($\Delta G^{\circ\prime}_{PEP} = 58$ kJ/mol, $\Delta G^{\circ\prime}_{ATP} = 29$ kJ/mol) (*3*). Without a sufficient supply of oxygen from respiration, tumor cells rely heavily on ATP production via the glycolytic cycle and hence pyruvate kinase (*2*).

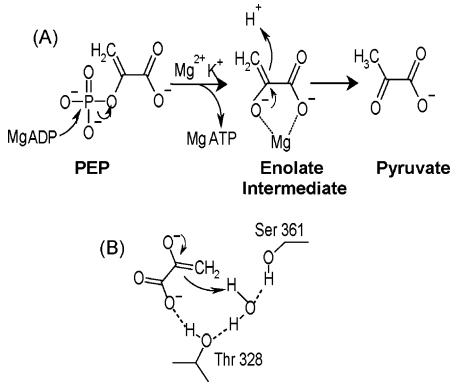

FIGURE 1: The pyruvate kinase reaction. (A) The reaction mechanism takes place in two steps and involves the formation of an enolate intermediate. (B) Proposed hydrogen-bonding scheme (based on this work) responsible for the protonation of the enolate. Additional water molecules may also hydrogen-bond to the crystallographically observed water to complete a hydrogen-bond network. However, these waters are not observed in the crystal structure and are therefore not depicted in this diagram. The metal ion used may also affect the reactivity of this water molecule as the proton donor.

Pyruvate kinase also regulates the supply of glycolytic phosphometabolites used as synthetic precursors in cellular proliferation. The down regulation of PK allows for the

[†] This research is funded by a grant from the American Heart Association (No. 0235416Z).

[‡] X-ray coordinates for human pyruvate kinase M2 have been deposited in Brookhaven Protein Data Bank under PDB No. 1T5A.

* Address correspondence to this author at Center for Pharmaceutical Biotechnology, University of Illinois at Chicago, 900 S. Ashland Ave, Chicago, IL 60607. E-mail, mesecar@uic.edu; phone, (312) 996-1687; fax, (312) 413-9303.

[1] Abbreviations: PK, pyruvate kinase; hPKM2, human pyruvate kinase M2; hPKR, human pyruvate kinase R; FBP, fructose-1,6-bisphosphate; PEP, phosphoenolpyruvate; NBSD201, 3-(1-pyridinio)-1-propanesulfonate; OTG, 1-*S*-octyl-*β*-D-thioglucopyranoside; DTT, dithiothreitol; EDTA, ethylenediaminetetraacetic acid.

10.1021/bi0474923 CCC: $30.25
Published on Web 06/15/2005

FIGURE 2: Multiple sequence alignment of the C-domain for all four human isozymes (hPK-R, L, M1, M2) and rabbit muscle M1 (RabPK-M). The amino acid residues that are 100% conserved among the human isozymes are shaded gray. The amino acid residues involved in the binding of FBP are indicated with an asterisk. The 56 amino acids that are encoded in exons 9 and 10 are underlined.

phosphometabolite pools preceding the pyruvate kinase reaction to accumulate and be channeled into synthetic processes (*4*). However, activation of PK increases ATP concentrations in the cell. As a result, one of the important keys to controlling tumor growth lies in the regulation of pyruvate kinase.

There are four isozymes of PK in humans. The R and L isozymes are encoded by the L gene and arise through the use of different tissue-specific promoters. The R isozyme is expressed in erythrocytes, and the L isozyme is expressed in liver (*5*). The L and R isozymes are both feed-forward regulated by the upstream metabolite fructose-1,6-bisphosphate (FBP). Mutations in the R and L isoforms are associated with nonspherocytic hemolytic anemia and jaundice, respectively (*6*, *7*). The M1 and M2 isoforms are encoded by the M gene and result from the alternative splicing of exons 9 and 10. These exons encode a stretch of 56 amino acids that have amino acid differences between the human M1 and M2 isoforms in 22 positions (*8*) (Figure 2). These amino acid differences are shown in Figure 3, and they are concentrated near the binding site for the allosteric regulator FBP.

The M1 isoform is expressed in skeletal muscle and brain tissue and is not allosterically regulated by FBP. The M2 isoform is expressed in fetal tissue and is allosterically regulated by FBP. As cells differentiate, the M2 isoform is progressively replaced by the remaining three isoforms. However, in tumorous cells, the M2 isoform is once again reexpressed and has therefore been designated as tumor-specific pyruvate kinase (hPKM2) (*9*). The M2 isozyme was initially discovered in a hepatoma cell line, and elevated levels of this isozyme have been observed in numerous cancerous cells (*10*−*12*). It has been investigated as a potential tumor marker in a variety of malignancies including GI cancers (particularly gastric, colorectal, and bile duct), rheumatic diseases, lung cancer, breast cancer, neuroendocrine tumors, urological malignancies, renal cell carcinoma, diabetic nephropathy, hematological malignancies, prostate cancer, and thyroid carcinoma (*13*−*28*). hPKM2 has been found to be a valuable tumor marker for GI cancers, rheumatic diseases, lung cancer, and breast cancer, and as a result, it is being used in commercial diagnostic assays for various cancers (*15*−*20*). These facts emphasize the importance of understanding the structure and regulatory properties of this enzyme.

The importance of M2 for cancer cell proliferation makes it an intriguing molecular target for the exploration and development of anticancer compounds. Moreover, since human pyruvate kinase isozymes have highly conserved active sites and disparate allosteric regulatory properties, they offer an opportunity to exploit the diversity between the allosteric sites for the discovery or design of ligands that can selectively regulate each of the PK isoforms (*29*). We report herein on the X-ray structure for hPKM2 complexed with FBP, K^+, Mg^{2+}, oxalate, and PO_4^{3-} and have analyzed it for unique structural characteristics relative to other known isoforms.

MATERIALS AND METHODS

Enzymes and Biochemicals. The enzymes *DNase*I and *Pfu* polymerase were purchased from Sigma, Inc. Rabbit muscle lactate dehydrogenase was obtained from Roche Diagnostics, and all other enzymes were purchased from Fermentas. Crystallization chemicals as well as the NBSD201 (3-(1-pyridinio)-1-propanesulfonate) were from Fluka. The sucrose used in the media was obtained from Acrôs Organics, and the OTG (1-*S*-octyl-*β*-D-thioglucopyranoside) was from Anatrace Chemicals. All other common chemicals were purchased from either Sigma or Fisher Scientific.

hPKM2 Expression Plasmids. The recombinant plasmid for the $(his)_6$-tagged hPKM2 enzyme was constructed by PCR amplification of the human pyruvate kinase M2 gene from the plasmid pCJ11 (*30*). The oligonucleotide primers used for PCR were synthesized by Sigma-Genosys and were designed to compliment the Topo-cloning system from Invitrogen. The forward primer, 5′-CACCATGTCGAAGCCCCATAC TCAA-3′, and the reverse primer, 5′-TCACGGCACAGGAACAACACGCAT-3′, were used for the PCR amplification. The amplified gene insert was cloned into the pET-Topo 100D vector using the directional Topo-cloning kit from Invitrogen. The final construct includes a

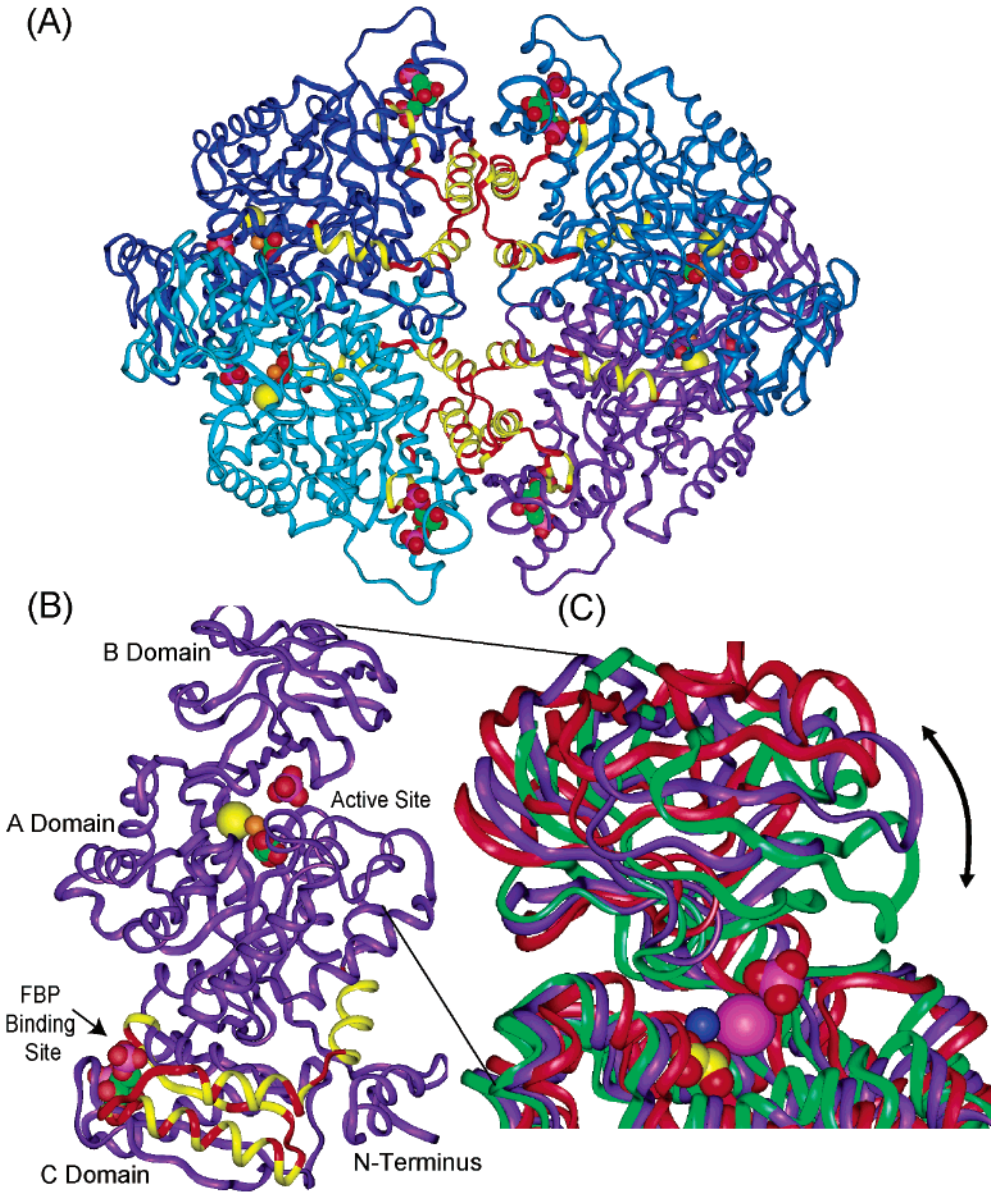

FIGURE 3: Structure of human pyruvate kinase M2 (hPKM2) highlighting the M1 and M2 differences. Ribbon diagrams of the hPKM2 tetramer (A) and monomer (B) displaying the four domains, N, A, B, and C. The 56 amino acid stretch that composes exons 9 and 10, which are alternatively spliced in the M1 and M2 isoforms, is colored yellow. The 24 amino acids that differ within this exon are shown in red. (C) An enlargement of the hPKM2 active site (purple) with the superimposed active sites of the rabbit muscle closed subunit (green) and open subunit (red).

36 amino acid N-terminal extension that contains the $(his)_6$ tag. This extension does not alter the kinetics of the enzyme (see Results). The entire gene sequence of the resulting plasmid (pJDAM-His) was verified by the RRC DNA sequencing facility at University of Illinois at Chicago (UIC).

A nontagged hPKM2 expression plasmid was constructed by PCR amplification of the gene from the pET-Topo construct described above. The oligonucleotide primers used for PCR were designed to consist of *Bam*HI and *Nde*I restriction sites flanking the gene. The following primers were used: forward, 5′-GCAGTCCATATGTTCGAAGCCCCATAG-3′; reverse, 5′-GCAGCTGGATCCTCACGGCACAGGAC-3′. The PCR-amplified gene inserts and the pET11a vector (Novagen) were digested by *Bam*HI and *Nde*I. The insert was ligated into the vector at an insert-to-vector ratio of 2:1. The entire gene sequence for the resulting vector (pJDAM) was verified by the UIC RRC DNA sequencing facility.

Overexpression and Purification of hPKM2. Rosetta pLysS cells (Novagen), a derivative of *Escherichia coli* BL21(DE3) tuner cells which contain rare tRNA codons that aid in the expression of human genes in bacteria, were transformed with pJDAM-His plasmid via electroporation. These cells were plated on LB agarose plates containing 100 μg/mL ampicillin. Single colonies were used to inoculate cultures that were grown in LB medium containing 100 μg/mL ampicillin and 34 μg/mL chloramphenicol at 37 °C overnight. The following day, the cells were transferred to 1 L of fresh media containing 5% (w/v) sucrose for a resulting optical density at 600 nm (OD600) of ~0.05. These cultures were then incubated at 37 °C until they reached an OD600 of 0.4. At this point, enzyme expression was induced by the addition of 1 mM isopropyl-β-D-galactopyranoside. After an ad-

ditional 3 h of growth at 37 °C, the cells were harvested, pelleted by centrifugation, and stored at −80 °C. The frozen cell pellets were resuspended in buffer A (50 mM Tris, pH 7.5, 0.1 M KCl, and 20% glycerol) containing one protease inhibitor tablet from Roche, 25 mM $MgCl_2$, and a minimal amount of DNaseI. The cells were lysed via sonication, the lysate was centrifuged, and the supernatant was discarded. Next, the pellet was washed with 1% OTG in 50 mM Tris, pH 7.5, this solution was centrifuged, and the supernatant was discarded. Resuspension buffer (6 M guanidine·HCl, 50 mM Tris, pH 8.0, and 10 mM imidazole) was used to resuspend the resulting pellet containing the inclusion bodies. Insoluble impurities were removed by centrifugation. The denatured protein solution was loaded onto a high-trap affinity column charged with Ni^{2+} (Amersham Biosciences). The protein was eluted in the resuspension buffer using a gradient of 10−500 mM imidazole. Fractions containing hPKM2 were collected, and DTT was added to a final concentration of 25 mM. The protein solution was diluted 1:10 by the dropwise addition of the protein via syringe into the refolding buffer (50 mM Tris, pH 8.0, 0.1 M KCl, 20% glycerol, 0.1 M EDTA, 1 mM DTT, and 0.1 M NBSD201). The solution was stirred for 2 min past addition and then allowed to incubate at room temperature overnight. The diluted refolding solution containing the protein was concentrated using Millipore Centricons MWCO 10 000 and then passed through a HiPrep desalting column (Pharmacia) equilibrated with Buffer A. The protein was then concentrated to ∼1 mL using Centricons. The concentrated protein was loaded onto a size-exclusion Superdex200 HR 26/60 column (Amersham Biosciences) equilibrated with Buffer A. The active protein fractions were pooled and concentrated down to ∼15 mg/mL using Centricons. The protein was stored at 4 °C.

Protein concentration during the purification was determined using the Bio-Rad Bradford Protein Assay. The purified enzyme concentration was determined by measuring the absorbance of the protein at 280 nm and using an extinction coefficient of 30 490 M^{-1} cm^{-1} (0.52 L/(g·cm)) that was experimentally determined (*31*).

The native protein was purified to homogeneity following the same protocol as that for the $(his)_6$-tagged enzyme with the omission of the high-trap affinity column and the addition of an anion-exchange column.

Enzyme Kinetics. Pyruvate kinase activity was determined using the lactate dehydrogenase, NADH coupled assay (*32*). The standard activity assay was performed in a 1.00 mL reaction volume and at 32 °C. The standard assay mixture contained 5 mM PEP, 5 mM ADP, 5 mM FBP, 15 mM $MgCl_2$, 200 mM KCl, and 175 μM NADH in 50 mM Bis Tris Propane, pH 8.0, with 25% glycerol.

Initial velocity versus substrate concentration curves for each substrate were measured by fixing all other substrate and ligands at saturating concentrations while varying the concentration of the desired substrate or ligand. Kinetic studies were performed in the absence and presence of 2 mM FBP, which resulted after a 1- to 50-fold dilution of the enzyme that was preincubated with 100 mM FBP at 4 °C. The kinetic parameters (V_{max}, K_m, K_I, and n_H) were fit to Michaelis−Menten, Hill, and competitive inhibition equations using the nonlinear regression program Sigma Plot with the Enzyme Kinetics module (SPSS Scientific). The K_I value is the dissociation constant of the inhibitor from the enzyme−inhibitor complex.

Table 1: Data Collection and Refinement Statistics

Data Collection	
space group	$P2_12_12_1$
unit cell (Å)	108.2, 145.0, 159.3
resolution (Å)	2.82
no. reflections observed	714 623
no. unique reflections	62 359
R merge (%)	11.3 (54.2)
$I/\sigma I$	12.1 (1.7)[a]
% completeness	96.6 (93.0)[a]
Refinement	
resolution range	20−2.82
no. reflections in working set	57 057
no. reflections in test set	2860
R_{cryst} (%)	23.4
R_{free} (%)	27.7
average *B*-factor (Å^2) (protein)	63.5
no. water molecules	136
rmsd from ideal geometry	
bond lengths (Å)	0.008
bond angles (deg)	1.2
Ramachandran plot	
allowed (%)	98.8
generous (%)	0.8
disallowed (%)	0.4

[a] The last resolution shell 2.90−2.82 Å is shown in parentheses.

Crystallization and X-ray Data Collection. Initial crystallization conditions for the $(his)_6$-tagged hPKM2 complex were determined from the PEG/Ion screen (Hampton Research) using hanging drop vapor diffusion trials at room temperature. These crystallization conditions were then optimized by fine gridding around the initial conditions until one condition produced well-diffracting crystals. A single crystal of human pyruvate kinase complexed with K^+, Mg^{2+}, oxalate, phosphate, and FBP was grown at 4 °C using hanging drop vapor diffusion with 4 mg/mL protein in 0.1 M KCl, 5 mM $MgCl_2$, 5 mM FBP, 5 mM ATP, 2 mM oxalate, and 20% glycerol. The well solution consisted of 0.04 M $(NH_4)_2HPO_4$, 20% glycerol, and 20% PEG 3350 at pH 8.0. The crystal was a diamond-like plate, about 10 μm × 100 μm × 100 μm, and grew within 2−3 weeks. Numerous crystals of native hPKM2 were screened by X-ray diffraction. Unfortunately, we were unable to identify native crystals that diffracted beyond 4.0 Å.

X-ray data were collected on SER-CAT Beamline 22-ID-B at the Advanced Photon Source (Argonne National Laboratory). The crystal was plunged into liquid nitrogen, and data were collected at 100 K using a MAR 225 detector. A total of 180 one-degree rotation X-ray images were collected with 2 s exposures at a wavelength of 0.92 Å and a crystal-to-detector distance of 250 mm. Data collection statistics are summarized in Table 1. The hPKM2 enzyme crystallized in space group $P2_12_12_1$ with unit cell dimensions of $a = 108.2$ Å, $b = 145.0$ Å, $c = 159.3$ Å. A Matthews coefficient of 2.5 Da/Å^3 is calculated using a full tetramer in the asymmetric unit.

Molecular Replacement. The initial phases for hPKM2 were determined by the method of molecular replacement using the program EPMR (Evolutionary Programming Molecular Replacement) (*33*). The search model used for molecular replacement consisted of a monomer from the rabbit muscle M1 pyruvate kinase structure (PDB: 1A49)

with all side chains intact. The final and optimal molecular replacement solution contained all four monomers of the tetramer and had a correlation coefficient of 0.626 using a resolution range of 9−5 Å.

Structure Refinement. Iterative rounds of positional and *B*-factor refinement were performed with CNS (Crystallography & NMR System), using a maximum-likelihood target function and structure factor amplitudes, and employing a sigma cutoff of 2. SigmaA, FOM-weighted electron density maps were created in CNS, and manual rebuilding was performed with the program O (*34*, *35*). Rigid body refinement was initially performed and resulted in an R_{cryst} of 0.47. Further refinement was performed by positionally restraining the four subunits by noncrystallographic symmetry (NCS) in CNS. Initially, the N-terminus, C-terminus, and the B-domain (residues 117−218) were excluded from NCS restraints due to high rms deviations among the subunits. Two groups, residues 22−106 and residues 222−500, in each of the four subunits A−D, were chosen to be restrained by NCS with an effective force-constant for positional restraints of 100 Kcal·mol^{-1}·A^{-2}.

The B-domain was rebuilt using the original B-domain from the rabbit muscle M1 model as a guide (*1*). Large regions of the B-domain were simultaneously rotated to simulate a hinge motion of the domain and positioned into the electron density. All four B-domains were found in approximately the same conformation. After four rounds of minimization, the NCS restraints were expanded to cover the entire molecule, including the B-domain, and the force constant was increased to a value of 500. The final rms deviations between the four subunits were A−B 0.046, A−C 0.048, and A−D 0.046.

In the final stages of model building, a composite-omit map was calculated to check for any model bias. The map was calculated by omitting ~7.5% of the model at a time, and model bias was unobserved. The final model was validated using Procheck, MolProbity, and WhatCheck (36−38). The resulting R_{free} and R_{cryst} values were 27.8% and 23.1%. The final refinement statistics for the hPKM2 model are displayed in Table 1, and the final model coordinates were deposited in the Protein Data Bank under PDB no. 1T5A (39). Figures of structures were produced using the programs Insight II and O (*35*, *40*).

RESULTS

Purification of hPKM2. The purification of hPKM2 involved the refolding of the enzyme from inclusion bodies. Typically, renaturation protocols utilize dialysis to gradually remove denaturing agents. However, to preserve costly reagents necessary for a large scale dialysis, protein refolding was achieved by a 1:10 dilution into a refolding buffer followed by removal of the residual denaturing agents via a rapid desalting column. After the initial renaturation protocol was refined and enzymatic activity was regained, a small scale dialysis was attempted to test which protocol yielded the greatest recovery of active enzyme. The use of the desalting column not only expedited the purification by 1 day, but it also produced enzyme with a higher specific activity (data not shown). Therefore, this refolding method proved successful in regaining highly active hPKM2 with a specific activity of ~200 units/mg, which is comparable to the previously reported specific activity for hPKM2 (*32*). An SDS−PAGE analysis of the hPKM2 purification is shown in Figure 4, and the final protein is judged to be over 95% pure. Each liter of culture yields 3−6 mg of purified active protein. The overexpression and purification of the native protein from 1 L of culture yield approximately 15 mg of active protein (data not shown).

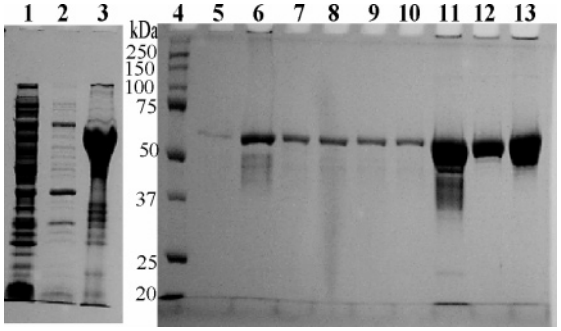

FIGURE 4: SDS−PAGE analysis of the hPKM2 purification. The molecular weight of $(his)_6$-tagged hPKM2 is ~60 kDa. Lanes: (1) soluble lysate, (2) 1% OTG wash, (3) inclusion body fraction, (4) protein standard (Bio-Rad Precision Plus), (5) refolding buffer, (6) concentrated refolding buffer, (7−9) desalted fractions, (10) combined desalted fractions, (11) concentrated desalted fractions, (12) Superdex 200 fractions pooled, and (13) concentrated and purified hPKM2.

Table 2: Kinetic Parameters for PEP and ADP in the Presence (+) and Absence (−) of FBP[a]

	FBP	K_m (mM)	V_{max}	n_H
ADP	+	0.24 ± 0.03	214 ± 6	1.0[b]
	−	0.34 ± 0.02	253 ± 6	1.0[b]
PEP	+	0.17 ± 0.01	218 ± 4	1.0[b]
	−	2.1 ± 0.7	310 ± 37	1.6 ± 0.1[c]

[a] Kinetic assays were carried out at 32 °C at pH 8.0 with saturating concentrations of [PEP] = 5 mM, [ADP] = 5 mM, [KCl] = 200 mM, and [$MgCl_2$] = 15 mM in the presence or absence of 2 mM FBP. In the presence of FBP, the enzyme was preincubated with 100 mM FBP at 4 °C before a 1:50 dilution into the assay mixture for kinetic analysis. [b] Kinetic data were best fit by the Michaelis−Menten equation. [c] Kinetic data were best fit by the Hill equation.

Kinetic Characterization of hPKM2. Kinetic studies were performed at 32 °C because numerous in vivo studies on cancer cells using animal models have shown that the temperature of a tumor is slightly below that of the normal ambient body temperature of 37 °C. Moreover, tumor cells tend to fall within the range of 31−33 °C in vivo (*41*). A pH value of 8.0 was chosen because this corresponds to the crystallization conditions for the crystal used for structure determination. Since the kinetic parameters for the $(his)_6$-tagged enzyme were identical within experimental error to the native hPKM2 enzyme (data not shown) and the $(his)_6$-tagged enzyme produced crystals that diffracted X-rays to a 2.8 Å resolution, all of the results presented below are for the $(his)_6$-tagged enzyme.

The kinetic parameters for PEP and ADP were determined in the presence and absence of the allosteric activator FBP, and the results were summarized in Table 2. In the absence of FBP, the K_m value for PEP is 2.7 mM and its interaction with hPKM2 exhibits positive cooperativity (n_H = 1.6). In the presence of saturating concentrations of FBP (2 mM), the K_m value for PEP decreases approximately 12-fold to a

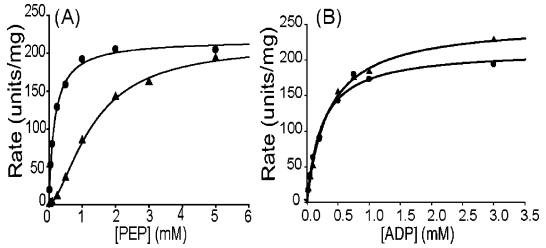

FIGURE 5: Steady-state kinetics for PEP and ADP in the absence and presence of FBP for $(his)_6$-tagged human PKM2. Kinetic measurements were performed at 32 °C and pH 8.0 with concentrations of [KCl] = 200 mM and [$MgCl_2$] = 15 mM in the presence or absence of 2 mM FBP. For experiments with FBP, the protein was preincubated with FBP at 4 °C before measurements were made. (A) Initial velocity versus [PEP] saturation curves varying PEP concentration with [ADP] = 5 mM in the absence (▲) and presence (●) of 2 mM FBP. (B) Initial velocity versus [ADP] saturation curves varying ADP concentration with [PEP] = 5 mM in the absence (▲) and presence (●) of 2 mM FBP.

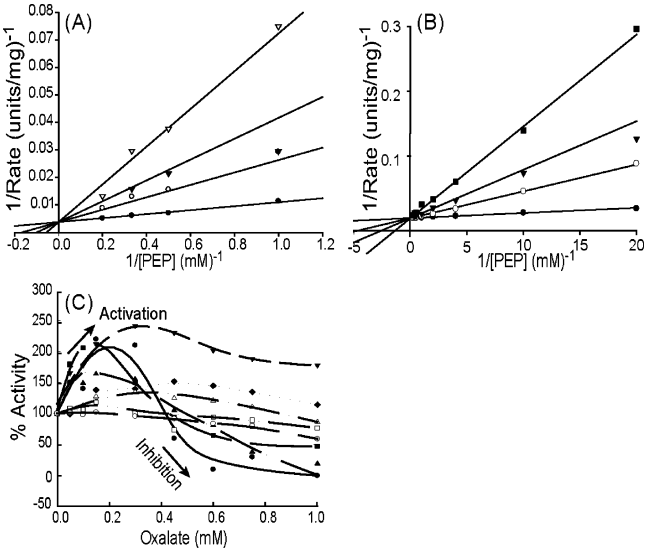

FIGURE 6: Oxalate activation/inhibition in the presence and absence of FBP. (A) Lineweaver−Burk plot for oxalate inhibition of hPKM2 in the absence of FBP varying [PEP] with [ADP] = 5 mM and various concentrations of oxalate; (●) 0 mM, (○) 0.4 mM, (▼) 0.8 mM, (▽) 1.6 mM. The V_{max} is 285 units/mg and the K_I for oxalate is 0.22 ± 0.06 mM. (B) Lineweaver−Burk plot for oxalate inhibition in the presence of 2 mM FBP varying [PEP] with [ADP] = 5 mM with oxalate concentrations of (●) 0 mM, (○) 0.1 mM, (▼) 0.2 mM, (■) 0.4 mM. The V_{max} is 227 units/mg and the K_I for oxalate is 0.024 ± 0.004 mM. (C) Oxalate titration curve for hPKM2 at various PEP concentrations in the absence of FBP. Oxalate activates at low PEP concentrations and then inhibits at higher PEP and oxalate concentrations. [PEP] = (●) 0.005 mM, (■) 0.05 mM, (▲) 0.25 mM, (▼) 0.5 mM, (◆) 0.75 mM, (△) 1.0 mM, (□) 2.0 mM, (○) 5.0 mM.

value of 0.17 mM and the positive cooperativity of PEP is abolished (n_H = 1.0). In contrast, in both the absence and presence of saturating FBP, the interaction of ADP with hPKM2 exhibits no cooperativity; that is, a hyperbolic response is observed (Figure 5), and the K_m values for ADP are nearly identical (Table 2). The maximal velocity of the hPKM2-catalyzed reaction decreases slightly in the presence of saturating FBP (see Table 2 and Figure 5), and the decrease, although small, is reproducible and may indicate a slight shift in the rate-determining step (*42*). The same FBP effect has been observed with the yeast enzyme (*43*).

Oxalate is a structural analogue of the enolate of pyruvate, and it acts as a simple, competitive inhibitor of hPKM2 in the presence of saturating FBP (Figure 6). The Lineweaver−Burk plots displayed in Figure 6 demonstrate that oxalate binding is competitive with PEP as indicated by the intersection on the *y*-axis. The K_I for oxalate was determined to be approximately 220 μM in the absence of FBP and 24 ± 4 μM in the presence of 2 mM FBP. The 10-fold decrease in the K_I for oxalate in the presence of FBP mimics the 12-fold decrease in K_m for PEP in the presence of FBP.

The inhibitory effects of oxalate are more complicated in the absence of FBP. At low, subsaturating concentrations of PEP, oxalate in low concentrations, for example, below 0.4 mM, activates the enzyme (Figure 6C). However, as PEP concentrations increase and all of the active sites are saturated by PEP, oxalate then directly competes with PEP for the active site. Oxalate binding to hPKM2 appears to induce the same conformational changes associated with the binding of the natural substrate PEP. Oxalate activation of the liver and erythrocyte PK isozymes in the absence of FBP has also been observed (*44*), and phosphoglycolate, a competitive inhibitor of the yeast enzyme, also activates the enzyme at low concentrations of PEP (*45*).

Overall Structure and Stability of hPKM2. Each monomer of pyruvate kinase consists of four domains that are designated as A, B, C, and N (Figure 3B). The tetramer is a dimer-of-dimers with approximate D_2 symmetry. The intermolecular subunit contacts for the first dimer occur between the A-domains of each monomer. The tetramer is then formed via dimerization along the C-subunit interfaces of each dimer (Figure 3A). The A-domain, composed of residues 44−116 and 219−389, is the core of the monomer and has an α_8/β_8 barrel tertiary structure motif. A combination of β-sheets and random coils make up the highly mobile B-domain that consists of a stretch of residues between Pro 117 and Pro 218. The active site of hPKM2 lies within a cleft formed between the A- and B-domain. The C-domain, composed of residues 390−531, consists of both α and β structural elements. The allosteric FBP-binding pocket is located entirely within the C-domain (*45*). The N-terminus is a small domain that is composed of residues 1−43. It consists of a helix-turn-helix motif that is preceded by a short stretch of residues, 1−12, as well as additional amino acids from the $(his)_6$-tag construct that were too disordered to build into the final model.

Pyruvate kinase isolated from several organisms, for example, yeast, hPKR, and hPKM2, requires 10−20% glycerol to stabilize the enzyme and prevent inactivation (*46*). However, structural evidence for specific binding sites of glycerol on pyruvate kinase has not yet been reported. Purification and crystallization of hPKM2 was performed in the presence of 20% glycerol. A thorough review of $F_o - F_c$ difference electron density maps, produced near the end of structural refinement, resulted in the identification of a number of strong (>4σ) positive features in density maps that were indicative of glycerol molecules. There are five glycerol molecules per hPKM2 monomer which are conserved in the same location between all four subunits. A total of 20 glycerol molecules were built into residual electron density in the hPKM2 tetramer (Figure 7). Three of the five conserved glycerols in each subunit form one or

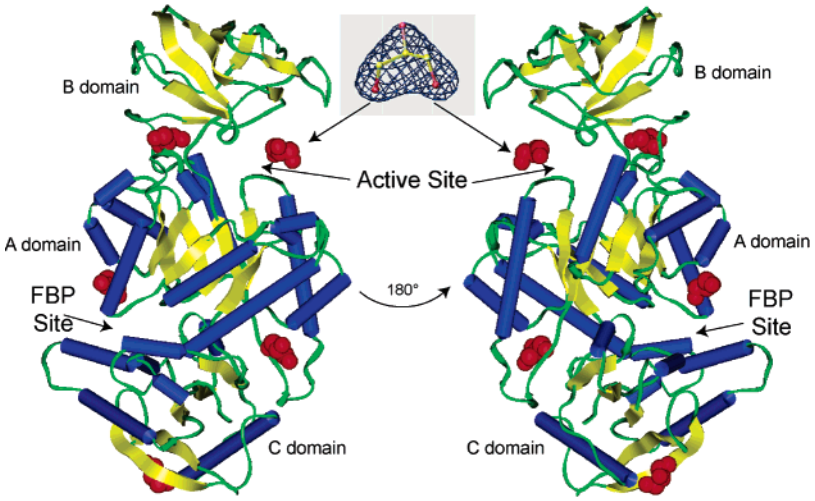

FIGURE 7: Glycerol-binding sites in hPKM2. The binding sites for the five glycerol molecules (red spheres) within a hPKM2 monomer are shown in relationship to the various domains of hPKM2 and to the FBP-binding site. The monomer (left side) was rotated approximately 180° (right side) to better illustrate the binding sites. For one of the glycerol molecules, a $2F_o - F_c$ omit map, contoured at 1.5σ, is shown as an inset. The same quality map is seen for all five glycerol molecules.

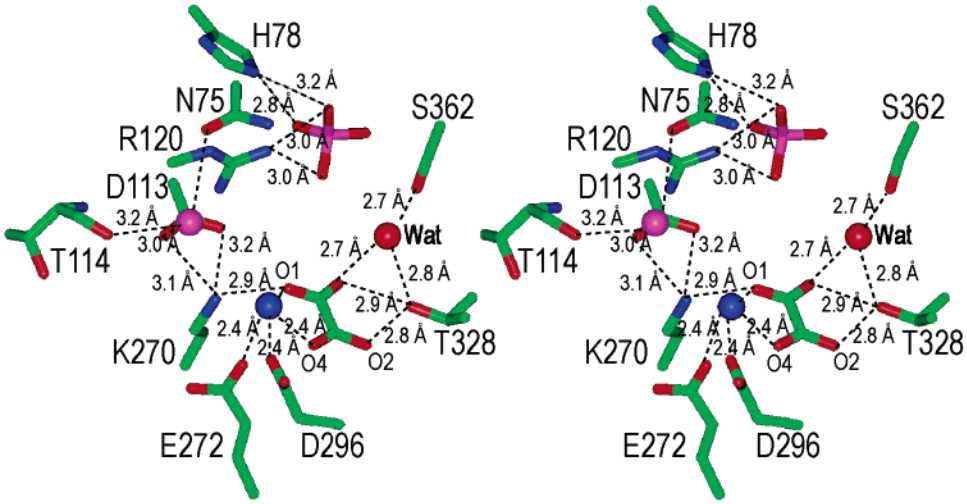

FIGURE 8: Interactions between hPKM2 and active site ligands. Mg^{2+}-oxalate, K^+, phosphate, and a water molecule are bound in the active site. Mg^{2+} (blue), K^+ (purple), and water (red) are shown as spheres.

more hydrogen bonds with the enzyme, while the remaining two in each subunit can be considered as having semirandom binding.

Active Site Structure and Mechanism of hPKM2. The pyruvate kinase reaction requires one monovalent cation, preferably K^+ or NH_4^+, and two divalent cations, preferably Mg^{2+} or Mn^{2+}, for catalysis. The amino acid residues that participate in catalysis, as well as the ligands oxalate, K^+, and Mg^{2+}, are bound in similar orientations as observed in other PK structures (Figure 8).

The pyruvate kinase reaction takes place in two steps (Figure 1). The first step involves a phosphoryl transfer from PEP to ADP forming an enolate intermediate and ATP, and the second step involves protonation of the enolate intermediate forming pyruvate (*47*). Lysine 270, which is 100% conserved among PK isozymes and was originally thought to be the proton donor, is proposed to promote the phosphoryl transfer step by stabilizing the pentavalent phosphate transition state (*48*). In hPKM2, the ϵ amino group of Lys 270 is positioned 2.9 Å away from the O1 oxygen atom of oxalate where phosphoryl transfer from PEP would take place (Figure 8). The active site K^+ atom, which may also serve to dissipate the developing negative charge during the phosphoryl transfer reaction, coordinates to the backbone carbonyl oxygen of Thr 114 (average value of 3.2 Å for all four subunits) and to one of the side-chain oxygen atoms of Glu 113 (3.0 Å). The Mg^{2+} ion is coordinated to the O1 and O4 oxygens of oxalate, as well as to two additional oxygens from the carboxyl side-chain groups of Glu 272 and Asp 296 (Figure 8). It is likely that additional water molecules fulfill the remainder of the octahedral coordination sphere for the magnesium ion, but electron density for these waters is not definitive.

Previous crystallographic structures of the rabbit muscle M1 enzyme show that the product ATP interacts with residues from both the A- and B-domain (*1*, *49*). Despite the presence of ATP in the crystallization buffer, it was not observed in the active site. However, inorganic phosphate, which was used as the crystallization buffer at a concentration of 40 mM, was observed in the active site in a position that would overlap where ATP would bind (*1*). The phosphate was found to bind with an occupancy of approximately 50%,

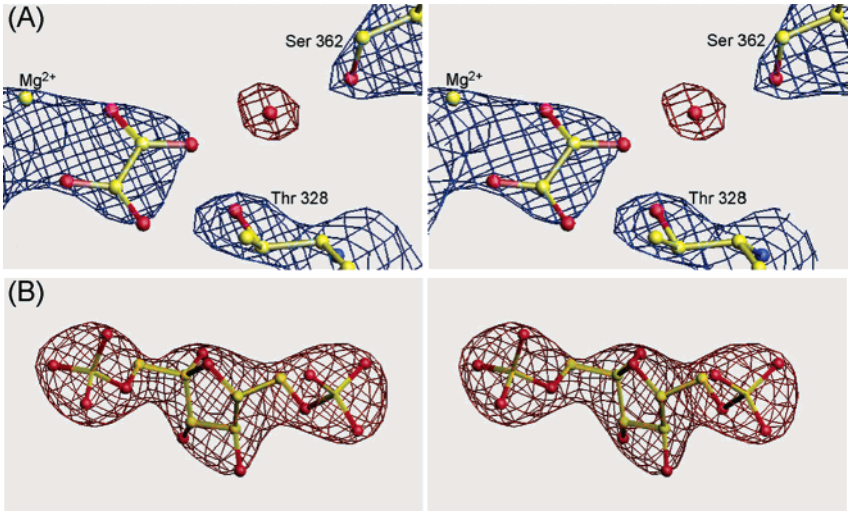

FIGURE 9: Stereoview electron density maps for hPKM2 ligands. (A) Active site electron density for Mg^{2+}-oxalate and the mechanistic water positioned on the 2-*si* face of the enolate analogue in subunit A. An $F_o - F_c$ omit map with the water molecule omitted from the Fourier synthesis contoured at 5σ is shown in red. A $2F_o - F_c$ map contoured at 2σ is shown in blue. (B) $F_o - F_c$ density map for the FBP bound in the allosteric site of subunit A is shown contoured at 7σ. Residues are labeled according to the hPKM2 structure numbering. The same quality maps are observed in all four active sites of the tetramer in the asymmetric unit.

and the oxygens of the phosphate bridge the A- and B-domain by forming bonds with side chains of Arg 120 and His 78. The absence of the product ATP in the active site is most likely the result of direct competition between ATP and phosphate for the active site. Phosphate, in the concentration range used in our experiments (40 mM), has been shown to act as either an activator or inhibitor of muscle pyruvate kinases (*50*, *51*). Phosphate and fluorophosphate have also been shown to bind in the active site of muscle pyruvate kinase (*52*). Furthermore, Nowak has studied pyruvate kinase complexed with Mg^{2+}, oxalate, and phosphate using NMR spectroscopy and found that a quaternary structure exists at 0.9 mM oxalate and 40 mM phosphate (*53*). One alternative reason for the absence of ATP in the active site would be that it was hydrolyzed by hPKM2 as a result of an intrinsic ATPase activity of the enzyme. However, we believe this unlikely because the intrinsic ATPase activity is dependent on the presence of high concentrations of bicarbonate which were not included in the crystallization buffer (*54*).

Analysis of the active site structures of each of the four subunits of hPKM2 in the asymmetric unit reveals a conserved water molecule with strong, spherical electron density ($>4\sigma$) peaks in $F_o - F_c$ difference maps (Figure 9A). The water molecules in each subunit are positioned on the 2-*si* face of the enolate analogue oxalate. These water molecules are involved in a hydrogen-bonding network with Thr 328 (2.8 Å), Ser 362 (2.7 Å), and O3 of oxalate (2.7 Å), which represents the position where the ethylene carbon of enolpyruvate would be protonated (*55*).

The Allosteric Site of hPKM2. The orientation for the FBP molecule in the allosteric site was modeled into the electron density by sampling possible binding modes to determine which binding mode results in the best fit. The resulting electron density for the β-furanose form of FBP is shown in Figure 9B. The orientation that best fits the electron density is the same as that for the yeast structure, where the 6′-phosphate is directed toward the 432−437 loop of the allosteric site and the 1′-phosphate is orientated toward Trp 482 (*45*). However, the orientation of FBP in the hPKM2 and yeast allosteric sites is different than the orientation of the FBP in the structure of the human R enzyme (PDB: 1LIU) (*39*). In the R-structure, the FBP is modeled with a reversed binding mode with the FBP molecule rotated such that the 1′- and 6′-phosphates are switched. Some ambiguity of the position of FBP in the R-structure is noted because the authors state that the position of FBP in the allosteric site of R is identical to that of the yeast enzyme (*56*).

The important interactions between FBP and the hPKM2 enzyme are shown in Figure 11. The 6′-phosphate oxygens of FBP hydrogen-bonds to several backbone amides including Lys 433, Ser 434, Ser 437, and Gly 520. The 1′-phosphate interacts with the side-chain guanidinium group of Arg 489, as well as with the backbone amide of Gly 518 and the indole ring nitrogen of Trp 482. The O3′ and O4′ hydroxyls of FBP form H-bonds with the backbone amides of Phe 521 and Gly 514. Several of these interactions are a result of the orientation of the FBP-activating loop. Simultaneously, the two residues preceding the loop, Trp 515 and Arg 516, are also orientated toward the binding pocket in both the hPKM2 and hPKR enzymes with FBP bound. However, in the rabbit muscle structure that does not bind FBP these residues are rotated away from the binding pocket, pointing toward the intersubunit contacts (Figure 10).

Ligand-Induced Domain Closure. The B-domain is highly mobile and undergoes a hinge bending motion, moving either toward or away from the A-domain, changing the size of the active site cleft (*57*). The A- and B-domain are connected by two strands each containing a proline (Pro 117 and Pro 218) residue at the pivotal point between the domains. Larsen et al. have shown that bound Mg^{2+}-ATP induces the closure of the active site, where the B-domain moves toward the A-domain and reduces the volume of the active site. The absence of Mg^{2+}-ATP results in an open conformation of the active site (*1*). The presence of phosphate in the active site and FBP in the allosteric site of all four subunits of the hPKM2 structure, results in a partially closed conformation of the active site in comparison to the open and closed conformations of the rabbit muscle (Figure 3C).

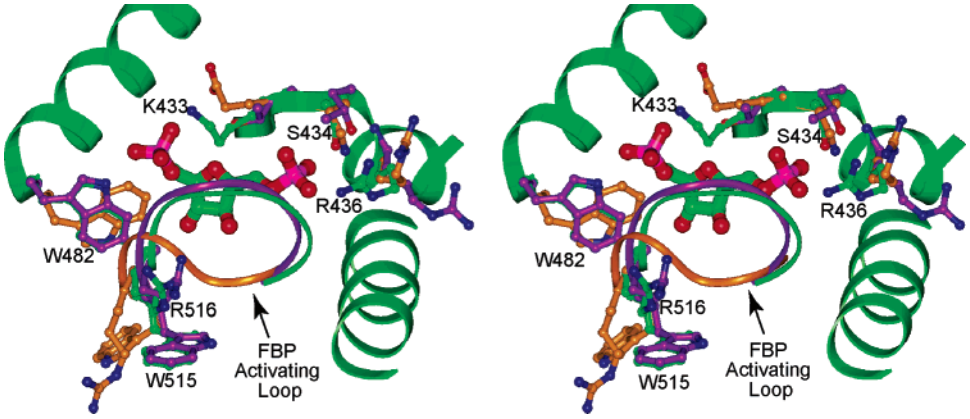

FIGURE 10: Stereoview of the FBP allosteric site. Superposition of the rabbit muscle (orange), human R (purple), and human M2 (green) PK structures showing the structural differences between the allosteric sites of the isozymes. The FBP-activating loop, as well as the preceding residues Trp 515 and Arg 516, are rotated toward the FBP in both the R and M2 allosteric sites with FBP bound.

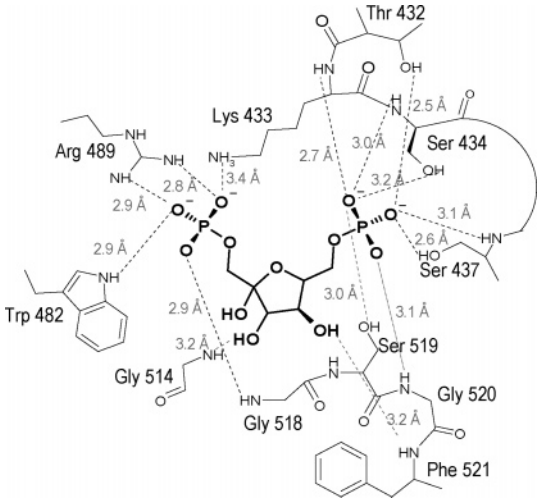

FIGURE 11: The allosteric site interactions with FBP. Schematic representation of the allosteric site binding interactions and their corresponding distances.

To analyze and quantitate the degree of ligand-induced closure of the active site, two distances within the cleft were measured for the open and closed conformation of rabbit muscle M1 and compared to the human M2 and human R structures. First, Cα carbons (residues Thr 129 and Pro 53) from both the A- and B-domain at the edge of the cleft furthest from the hinge axis were used to indicate the greatest distance between the A- and B-domain. Second, the Cα atoms for a pair of residues (Asp 178 and Asp 296) close to the hinge axis were selected to more fully describe the overall movement of the B-domain. The distances for the open and closed conformations of the rabbit muscle structure are listed in Table 3, along with the distances for the partially closed hPKM2 and hPKR structures.

To further describe the domain motions, the various conformations were analyzed using the DynDom program, which can identify individual domains in proteins and determine hinge axes and hinge-bending residues (*58*). The DynDom program is able to analyze conformational differences between two proteins and then provide a measure of the degree of rotation and translation about the determined hinge axis between two domains so that one can fully characterize the conformational differences observed (*59*). The A- and B- domain from hPKM2, hPKR, and rabbit M1-open subunits were analyzed relative to the closed conformation of the rabbit M1 enzyme. The rotational and translational differences between the B-domains for each of the PK isozymes were calculated, and the values in degrees and angstroms are summarized in Table 3. The implications of the differences in the rotation and translational values are discussed below.

DISCUSSION

Previous investigations to determine the identity of the proton donor that protonates the enolate intermediate in the second step of the PK reaction mechanism have examined various possibilities, but so far, definitive evidence for the proton donor has not yet been obtained (*60*). It has been determined that protonation occurs stereospecifically from the 2-*si* face of the enolate, and the X-ray structures of the yeast and rabbit muscle enzymes confirm that Lys 270 is not in an ideal position to be the proton donor (*45*, *61*). In addition, mutagenesis on Lys 270 indicates that it is involved directly in phosphoryl transfer (*48*).

Kinetic isotope effect studies and pulse−chase trapping experiments indicate that the proton donor is a monoprotic amino acid residue with a high pK_a that either rapidly exchanges with a proton from solvent or is a proton derived from a water molecule originating from bulk solvent (*62*, *63*). A proton relay system has been proposed to occur between several residues in the active site that are hydrogen-bonded to water molecules (*1*). One residue, Thr 328, forms a hydrogen bond with the O3 of oxalate that is ~2.7 Å (ranges from 2.3 to 3.0 Å in the four subunits) and has been proposed to be the direct proton donor. However, despite its vicinity to the substrate, mutagenesis studies indicate that Thr 328 is not the direct proton donor (*60*). Recently, proton inventory studies performed on mutants of yeast PK with this threonine (Thr 298 in yeast PK) mutated to an alanine, serine, and cysteine revealed that water is likely the active site proton donor and that Thr 328 plays a role in the activation of the water molecule (*60*, *64*). The conservation and location of the water molecule in the active sites of the hPKM2 and rabbit muscle enzymes, shown in Figures 8 and 9A, support previous biochemical results that this water molecule is involved in a hydrogen-bonding network that may function to transfer a solvent-derived proton to the enolate intermediate.

The high-resolution structure of the rabbit muscle enzyme in complex with Mg, oxalate, and Mg-ATP reveals two

Table 3: Ligand-Induced Closure of the Active Sites of PK isozymes[a]

	distances (Å)[b]		ligands bound[c]		relative to M1-closed[d]	
	P53 to T129	D178 to D296	active site*	allosteric site	rotation (deg)	translation (Å)
M1-open	23.9	8.0	-	-	40.5	−0.7
M1-closed	8.1	5.3	Mg^{2+}-ATP	-	-	-
M2	16.8	4.5	PO_4^{3-}	FBP	22.2	0.1
R	17.0	7.6	-	FBP	23.4	0.3

[a] Rabbit M1 distances for the open and closed conformation are measured from structure 1A49 published by Larsen et al. (*1*). [b] Distances are between the Cα carbons of indicated residues. [c] Ligands other than K^+, M^{2+}, and PEP substrate analogues bound in the active site. [d] Rotation and translation measurements between human hM2PK and rabbit muscle M1 PK were determined via the DyanDom program (*58*). The rabbit M1 enzyme in the closed conformation (1A49) was used as the reference point for the pivotal axis (defined for PK as residues 112−119 and 217−220). The rotation and translation values are determined by measuring the deviations between two structures parallel (rotation) and perpendicular (translation) to the hinge axis, which is defined by a line joining the centers of mass of the two domains (*59*).

additional water molecules in this hydrogen-bonding network that connect the active site water molecule observed in both the rabbit muscle and human PKM2 structures to a distant, yet conserved, Glu 363 (*1*). Unfortunately, these additional waters were not observed in our structure, perhaps because they are too mobile or simply have low occupancy. On the basis of these observations, we propose the hydrogen-bonding scheme shown in Figure 1B to illustrate how the protonation occurs via this conserved water molecule.

The most significant observable difference between the rabbit muscle M1 and the hPKM2 allosteric sites is the orientation of the FBP-activating loop, residues 517−521 (Figure 10). This loop surrounds the FBP molecule in the hPKM2 structure and essentially closes the allosteric site. The conformation of the FBP-activating loop in the human R enzyme, which is also bound with FBP, is similar to that of the hPKM2 FBP-activating loop. In the rabbit muscle M1 structure, which does not bind FBP, this loop is oriented away from the FBP-binding pocket toward the intersubunit contacts resulting in a more open conformation of the allosteric site (Figure 10).

In addition to the differences in orientation of the FBP-activating loop, other structural variations were observed. In the hPKM2 and hPKR structures, Trp 482 is rotated ∼180° about the $C_\beta-C_\gamma$ bond relative to the orientation of Trp 481 in the rabbit muscle enzyme, allowing for the formation of hydrogen-bond interactions between the indole ring nitrogen and a 1′-phosphate oxygen. Position 433 (hPKM2 numbering) has been implicated to be extremely influential in FBP binding (*65*, *66*). The amino acids in position 433 differ between all three, M2, M1, and R, PK isozymes from lysine to glutamate to threonine, respectively (Figure 10). Mutation of yeast Thr 403 to glutamate (analogous to position 433 in hPKM2) abolishes FBP binding (*65*). Similarly, the mutation of the glutamate in the M1, which normally does not bind FBP, to lysine engenders the enzyme to bind FBP (*66*). Therefore, the electrostatic properties of the side group that occupies position 433 play a prominent role in eliciting allosteric activation by FBP. More specifically, positively charged or neutral amino acids result in FBP activation, and negatively charged amino acids inhibit FBP activation.

The concept of ligand-induced closure of the active site of rabbit muscle M1 by Larsen et al. was expanded to show that the ligand-induced closures of the active site are not only dependent on ligands binding to the active site but are also dependent on ligands binding to the allosteric sites. Differences between the open and closed forms can be described as follows. The distance between Pro 53 and Thr 129 in the open conformation of the rabbit muscle enzyme is 23.9 Å, compared to a distance of only 8.1 Å for the closed conformation. These distances for both the human M2 (16.8 Å) and human R (17.0 Å) enzymes with FBP bound are approximately halfway between the open and closed conformations of the rabbit muscle enzyme. The distance between Asp 178 and Asp 296 in these isozymes reveals a shorter, but notable, difference and reflects a different and separate degree of closure. With Mg^{2+}-ATP or phosphate bound, this inner distance of the active site is approximately 5.0 Å. However, without either of these ligands bound, this distance is approximately 8.0 Å. Therefore, as ligands bind to different locations on the enzyme, they can induce intermediate states of closure around the active site. The varying states indicate that the motion of the B-domain deviates from a simple hinge motion between two rigid bodies.

This observation is further supported by the DynDom analysis which relates the rotation and translation of the B-domain about the hinge axis (defined for PK as residues 112−119 and 217−220) for the various conformational states of PK (*58*). The B-domain in the rabbit M1-open conformation is rotated 40.5° and translated −0.7 Å relative to the rabbit M1-closed conformation. The B-domain in the hPKR and hPKM2 structures is rotated by 23.4° and 22.2°, and translated by 0.3 Å and 0.1 Å relative to the rabbit muscle M1-closed conformation. The DynDom analysis confirms that these structures exhibit the partially closed conformation of the active site. The rotation about the hinge axis with an associated translation indicates a closure and twist motion between the two domains (*59*).

Monomers of PK associate and form dimers along the A−A′ interface. A pair of PK dimers associates via interactions along the C-domain near the FBP-binding site. The binding of FBP appears to alter the conformation of the FBP-activating loop, as well as the two residues preceding the FBP-activating loop, Arg 515 and Trp 516, which are directed toward the C−C′ subunit interface in the rabbit muscle M1 structure. These residues are rotated toward the FBP-binding pocket and away from the subunit interface in the hPKM2 and hPKR structures. Therefore, motions of the FBP-activating loop can influence intersubunit contacts along the C-domain, which may, in turn, cause each monomer to pivot about the A−A′ interface.

Rotations about the A−A′ subunit interface could affect Gly 295, which interacts with the neighboring subunit. Therefore, structural motions that occur at this subunit

interface near Gly 295 could directly alter the conformation of Asp 296, which coordinates the active site divalent cation, that is, the Mg^{2+} atom complexed with the enolate intermediate, and thereby influence metal binding. Thus, a structural link between metal binding and FBP activation is now established and supports previous kinetic and thermodynamic investigations on metal cation activation of pyruvate kinase (*53*, *67*−*70*).

Several structural variations in the FBP allosteric binding pocket are apparent and may offer an excellent opportunity to discriminate between the pyruvate kinase isoforms. In addition, glycerol-binding sites may offer an opportunity to discover novel small molecule compounds that can bind to PK and regulate or stabilize its activity. Similarly, the experimental approach to locate binding sites on protein surfaces using multiple solvent crystal structures (MSCS) has been successful in the design of inhibitors, such as the TFA-dipeptide-anilide inhibitors of elastase, that bind to novel allosteric sites (*71*). Allosteric binding pockets located away from the catalytic sites have been shown to be useful in regulating enzymatic activity. For example, small molecule compounds that bind to allosteric sites of tumor suppressor p53, hemoglobin, and inducible nitric oxide synthase affect the stability of the protein or alter the subunit association (*29*, *72*). The ability to stabilize the human R isoform of pyruvate kinase by the binding of compounds to these allosteric sites could aid in the restoration of PK activity in the red blood cells of patients with nonspherocytic hemolytic anemia caused by mutation in PK that results in decreased thermostability. Furthermore, thyroid hormone analogues are known to inhibit hPKM2 by stabilizing the monomeric, low activity, form of the enzyme (*73*). It is possible that these analogues do not bind in the active site or FBP-binding site but rather to one of the many available binding pockets in the hPKM2 structure. Therefore, analysis of the glycerol-binding sites and other potential binding pockets may prove useful for determining additional regulatory sites on pyruvate kinase.

In summary, the X-ray structure determination of hPKM2 has provided an opportunity to analyze structural variations among the PK isoforms for features that could eventually be used for drug design. Allosteric sites can provide excellent drug-design templates because they are usually more variable between species than highly conserved active sites (*29*). Previous computational docking studies with the yeast pyruvate kinase X-ray structure aimed at structure-based discovery of novel allosteric regulators have yielded three novel allosteric activators of yeast PK (*65*). Furthermore, structure-based drug design for novel hemoglobin regulators has led to the discovery of compounds that bind to or react at the allosteric site of hemoglobin, which have the potential for the treatment of sickle cell disease, brain tumors, hypoxia, ischemia, and trauma-related blood loss (*72*). Similar structure-based design studies on human PK may one day lead to allosteric drugs for the treatment of cancer and nonspherocytic hemolytic anemia (*71*).

ACKNOWLEDGMENT

We are grateful to Kiira Ratia for her help in constructing the native hPKM2 plasmid. We also thank Sheue-yann Cheng from the NIH for the original plasmid DNA pCJ11 for cloning. This research is funded by a grant from the American Heart Association (No. 0235416Z). Use of the Advanced Photon Source was supported by the U.S. Department of Energy, Office of Science, Office of Basic Energy Sciences, under Contract No. W-31-109-Eng-38. Data were collected at Southeast Regional Collaborative Access Team (SER-CAT) 22-ID (or 22-BM) beamline at the Advanced Photon Source, Argonne National Laboratory. Supporting institutions may be found at www.ser-cat.org/members.html.

REFERENCES

1. Larsen, T. M., Benning, M. M., Rayment, I., and Reed, G. H. (1998) Structure of the bis(Mg2+)-ATP-oxalate complex of the rabbit muscle pyruvate kinase at 2.1 Å resolution: ATP binding over a barrel, *Biochemistry 37*, 6247−55.
2. Mazurek, S., Boschek, C. B., and Eigenbrodt, E. (1997) The role of phosphometabolites in cell proliferation, energy metabolism, and tumor therapy, *J. Bioenerg. Biomembr. 29*, 315−30.
3. Mazurek, S., Grimm, H., Boschek, C. B., Vaupel, P., and Eigenbrodt, E. (2002) Pyruvate kinase type M2: a crossroad in the tumor metabolome, *Br. J. Nutr. 87* (Suppl. 1), S23−9.
4. Eigenbrodt, E., Reinacher, M., Scheefers-Borchel, U., Scheefers, H., and Friis, R. (1992) Double role for pyruvate kinase type M2 in the expansion of phosphometabolite pools found in tumor cells, *Crit. Rev. Oncog. 3*, 91−115.
5. Noguchi, T., Yamada, K., Inoue, H., Matsuda, T., and Tanaka, T. (1987) The L- and R-type isozymes of rat pyruvate kinase are produced from a single gene by use of different promoters, *J. Biol. Chem. 262*, 14366−71.
6. Cotton, F., Bianchi, P., Zanella, A., Van Den Bogaert, N., Ferster, A., Hansen, V., Van Herreweghe, I., Vertongen, F., and Gulbis, B. (2001) A novel mutation causing pyruvate kinase deficiency responsible for a severe neonatal respiratory distress syndrome and jaundice, *Eur. J. Pediatr. 160*, 523−4.
7. Larochelle, A., Magny, P., Tremblay, S., and Medicis, E. E. (1999) Erythropoiesis: pyruvate kinase deficiency which causes non-spherocytic hemolytic anemia: the gene and its mutations, *Hematology 4*, 77−87.
8. Noguchi, T., Inoue, H., and Tanaka, T. (1986) The M1- and M2-type isozymes of rat pyruvate kinase are produced from the same gene by alternative RNA splicing, *J. Biol. Chem. 261*, 13807−12.
9. Yamada, K., and Noguchi, T. (1995) Alteration of isozyme gene expression during cell differentiation and oncogenesis, *Nippon Rinsho 53*, 1112−8.
10. Kato, H., Fukuda, T., Parkison, C., McPhie, P., and Cheng, S. Y. (1989) Cytosolic thyroid hormone-binding protein is a monomer of pyruvate kinase, *Proc. Natl. Acad. Sci. U.S.A. 86*, 7861−5.
11. Obata, T., Fukuda, T., Willingham, M. C., Liang, C. M., and Cheng, S. Y. (1989) A cytoplasmic thyroid hormone binding protein: characterization using monoclonal antibodies, *Biochemistry 28*, 617−23.
12. Staal, G. E., and Rijksen, G. (1985) *Regulation of Carbohydrate Metabolism 1*, CRC Press, Boca Raton, FL.
13. Bena-Boupda, N. F., Rezai, S. S., Klett, R., Eigenbrodt, E., and Bauer, R. (2003) Value of tumor M2-PK in thyroid carcinoma: a pilot study, *Anticancer Res. 23*, 5237−40.
14. Hardt, P. D., Toepler, M., Ngoumou, B., Rupp, J., and Kloer, H. U. (2003) Measurement of fecal pyruvate kinase type M2 (tumor M2-PK) concentrations in patients with gastric cancer, colorectal cancer, colorectal adenomas and controls, *Anticancer Res. 23*, 851−3.
15. Schneider, J., Neu, K., Velcovsky, H. G., Morr, H., and Eigenbrodt, E. (2003) Tumor M2-pyruvate kinase in the follow-up of inoperable lung cancer patients: a pilot study, *Cancer Lett. 193*, 91−8.
16. Kim, C. W., Kim, J. I., Park, S. H., Han, J. Y., Kim, J. K., Chung, K. W., and Sun, H. S. (2003) Usefulness of plasma tumor M2-pyruvate kinase in the diagnosis of gastrointestinal cancer, *Korean J. Gastroenterol. 42*, 387−93.
17. Hoopmann, M., Warm, M., Mallmann, P., Thomas, A., Gohring, U. J., and Schondorf, T. (2002) Tumor M2 pyruvate kinase—determination in breast cancer patients receiving trastuzumab therapy, *Cancer Lett. 187*, 223−8.

18. Luftner, D., Mesterharm, J., Akrivakis, C., Geppert, R., Petrides, P. E., Wernecke, K. D., and Possinger, K. (2000) Tumor type M2 pyruvate kinase expression in advanced breast cancer, *Anticancer Res. 20*, 5077−82.
19. Schneider, J., Peltri, G., Bitterlich, N., Neu, K., Velcovsky, H. G., Morr, H., Katz, N., and Eigenbrodt, E. (2003) Fuzzy logic-based tumor marker profiles including a new marker tumor M2-PK improved sensitivity to the detection of progression in lung cancer patients, *Anticancer Res. 23*, 899−906.
20. Oremek, G. M., Muller, R., Sapoutzis, N., and Wigand, R. (2003) Pyruvate kinase type tumor M2 plasma levels in patients afflicted with rheumatic diseases, *Anticancer Res. 23*, 1131−4.
21. Schulze, G. (2000) The tumor marker tumor M2-PK: an application in the diagnosis of gastrointestinal cancer, *Anticancer Res. 20*, 4961−4.
22. Yilmaz, S., Ozan, S., and Ozercan, I. H. (2003) Comparison of pyruvate kinase variants from breast tumor and normal breast, *Arch. Med. Res. 34*, 315−24.
23. Roigas, J., Deger, S., Schroeder, J., Wille, A., Turk, I., Brux, B., Jung, K., Schnorr, D., and Loening, S. A. (2003) Tumor type M2 pyruvate kinase expression in metastatic renal cell carcinoma, *Urol. Res. 31*, 358−62.
24. Pezzilli, R., Migliori, M., Morselli-Labate, A. M., Campana, D., Ventrucci, M., Tomassetti, P., and Corinaldesi, R. (2003) Diagnostic value of tumor M2-pyruvate kinase in neuroendocrine tumors. A comparative study with chromogranin A, *Anticancer Res. 23*, 2969−72.
25. Oremek, G. M., Rutner, F., Sapoutzis, N., and Sauer-Eppel, H. (2003) Tumor marker pyruvate kinase type tumor M2 in patients suffering from diabetic nephropathy, *Anticancer Res. 23*, 1155−8.
26. Varga, Z., Hegele, A., Stief, T., Heidenreich, A., and Hofmann, R. (2002) Determination of pyruvate kinase type tumor M2 in human renal cell carcinoma: a suitable tumor marker?, *Urol. Res. 30*, 122−5.
27. Hegele, A., Varga, Z., Kosche, B., Stief, T., Heidenreich, A., and Hofmann, R. (2003) Pyruvate kinase type tumor M2 in urological malignancies, *Urol. Int. 70*, 55−8.
28. Oremek, G. M., Rox, S., Mitrou, P., Sapoutzis, N., and Sauer-Eppel, H. (2003) Tumor M2-PK levels in haematological malignancies, *Anticancer Res. 23*, 1135−8.
29. DeDecker, B. S. (2000) Allosteric drugs: thinking outside the active-site box, *Chem. Biol. 7*, R103−7.
30. Ashizawa, K., Willingham, M. C., Liang, C. M., and Cheng, S. Y. (1991) In vivo regulation of monomer-tetramer conversion of pyruvate kinase subtype M2 by glucose is mediated via fructose 1,6-bisphosphate, *J. Biol. Chem. 266*, 16842−6.
31. Pace, C. N., Vajdos, F., Fee, L., Grimsley, G., and Gray, T. (1995) How to measure and predict the molar absorption coefficient of a protein, *Protein Sci. 4*, 2411−23.
32. Imamura, K., and Tanaka, T. (1982) Pyruvate kinase isozymes from rat, *Methods Enzymol. 90*, 150−65.
33. Kissinger, C. R., Gehlhaar, D. K., and Fogel, D. B. (1999) Rapid automated molecular replacement by evolutionary search, *Acta Crystallogr., Sect. D 55*, 484−91.
34. Brunger, A. T., Adams, P. D., Clore, G. M., DeLano, W. L., Gros, P., Grosse-Kunstleve, R. W., Jiang, J. S., Kuszewski, J., Nilges, M., Pannu, N. S., Read, R. J., Rice, L. M., Simonson, T., and Warren, G. L. (1998) Crystallography & NMR system: a new software suite for macromolecular structure determination, *Acta Crystallogr., Sect. D 54*, 905−21.
35. Jones, T. A., Zou, J. Y., Cowan, S. W., and Kjeldgaard. (1991) Improved methods for building protein models in electron density maps and the location of errors in these models, *Acta Crystallogr., Sect. A 47*, 110−9.
36. Lovell, S. C., Davis, I. W., Arendall, W. B., III, de Bakker, P. I., Word, J. M., Prisant, M. G., Richardson, J. S., and Richardson, D. C. (2003) Structure validation by Calpha geometry: phi, psi and Cbeta deviation, *Proteins 50*, 437−50.
37. Laskowski, R. A., Rullmannn, J. A., MacArthur, M. W., Kaptein, R., and Thornton, J. M. (1996) AQUA and PROCHECK-NMR: programs for checking the quality of protein structures solved by NMR, *J. Biomol. NMR 8*, 477−86.
38. Vriend, G. (1990) WHAT IF: a molecular modeling and drug design program, *J. Mol. Graphics 8*, 52−6, 29.
39. Berman, H. M., Westbrook, J., Feng, Z., Gilliland, G., Bhat, T. N., Weissig, H., Shindyalov, I. N., and Bourne, P. E. (2000) The protein data bank, *Nucleic Acids Res. 28*, 235−42.
40. Accelrys Software, Inc. (2001−2004) http://www.accelrys.com.
41. Babsky, A., Hekmatyar, S. K., Wehrli, S., Nelson, D., and Bansal, N. (2004) Effects of temperature on intracellular sodium, pH and cellular energy status in RIF-1 tumor cells, *NMR Biomed. 17*, 33−42.
42. Ford, S. R., and Robinson, J. L. (1976) The proton-transfer reactions catalyzed by yeast pyruvate kinase, *Biochim. Biophys. Acta 438*, 119−30.
43. Kuczenski, R. T., and Suelter, C. H. (1971) Fructose 1,6-diphosphate enhances inactivation of yeast pyruvate kinase at 23°. Evidence for a stabilized dimer intermediate, *Biochemistry 10*, 2867−72.
44. Buc, H., Demaugre, F., and Leroux, J. P. (1978) The kinetic effects of oxalate on liver and erythrocyte pyruvate kinases, *Biochem. Biophys. Res. Commun. 85*, 774−9.
45. Jurica, M. S., Mesecar, A., Heath, P. J., Shi, W., Nowak, T., and Stoddard, B. L. (1998) The allosteric regulation of pyruvate kinase by fructose-1,6-bisphosphate, *Structure 6*, 195−210.
46. Ruwart, M. J., and Suelter, C. H. (1971) Activation of yeast pyruvate kinase by natural and artificial cryoprotectants, *J. Biol. Chem. 246*, 5990−3.
47. Robinson, J. L., and Rose, I. A. (1972) The proton-transfer reactions of muscle pyruvate kinase, *J. Biol. Chem. 247*, 1096−105.
48. Bollenbach, T. J., Mesecar, A. D., and Nowak, T. (1999) Role of lysine 240 in the mechanism of yeast pyruvate kinase catalysis, *Biochemistry 38*, 9137−45.
49. Lodato, D. T., and Reed, G. H. (1987) Structure of the oxalate-ATP complex with pyruvate kinase: ATP as a bridging ligand for the two divalent cations, *Biochemistry 26*, 2243−50.
50. Baranowska, B., and Baranowski, T. (1975) Pyruvate kinase from human skeletal muscle, *Mol. Cell. Biochem. 6*, 197−201.
51. Kuczek, M. (2002) Influence of inorganic pyrophosphate on the kinetics of muscle pyruvate kinase: a simple nonallosteric feedback model, *Biosystems 66*, 11−20.
52. Nowak, T. (1978) Structure of the fluorophosphate-pyruvate kinase complex investigated by 31P relaxation rate studies, *Arch. Biochem. Biophys. 186*, 343−50.
53. Nowak, T. (1978) Structural changes at the active site of pyruvate kinase during activation and catalysis, *J. Biol. Chem. 253*, 1998−2004.
54. Tietz, A., and Ochoa, S. (1958) Fluorokinase and pyruvic kinase, *Arch. Biochem. Biophys. 78*, 477−93.
55. Larsen, T. M., Laughlin, L. T., Holden, H. M., Rayment, I., and Reed, G. H. (1994) Structure of rabbit muscle pyruvate kinase complexed with Mn^{2+}, K^{+}, and pyruvate, *Biochemistry 33*, 6301−9.
56. Valentini, G., Chiarelli, L. R., Fortin, R., Dolzan, M., Galizzi, A., Abraham, D. J., Wang, C., Bianchi, P., Zanella, A., and Mattevi, A. (2002) Structure and function of human erythrocyte pyruvate kinase. Molecular basis of nonspherocytic hemolytic anemia, *J. Biol. Chem. 277*, 23807−14.
57. Gerstein, M., and Krebs, W. (1995) Database of macromolecular movements, http//molmovdb.org.
58. Lee, R. A., Razaz, M., and Hayward, S. (2003) The DynDom database of protein domain motions, *Bioinformatics 19*, 1290−1.
59. Hayward, S., and Berendsen, H. J. (1998) Systematic analysis of domain motions in proteins from conformational change: new results on citrate synthase and T4 lysozyme, *Proteins 30*, 144−54.
60. Susan-Resiga, D., and Nowak, T. (2003) The proton-transfer step catalyzed by yeast pyruvate kinase, *J. Biol. Chem. 278*, 12660−71.
61. Rose, I. A. (1970) Stereochemistry of pyruvate kinase, pyruvate carboxylase, and malate enzyme reactions, *J. Biol. Chem. 245*, 6052−6.
62. Rose, I. A., and Kuo, D. J. (1989) The substrate proton of the pyruvate kinase reaction, *Biochemistry 28*, 9579−85.
63. Rose, I. A., Kuo, D. J., and Warms, J. V. (1991) A rate-determining proton relay in the pyruvate kinase reaction, *Biochemistry 30*, 722−6.
64. Susan-Resiga, D., and Nowak, T. (2004) Proton donor in yeast pyruvate kinase: chemical and kinetic properties of the active site Thr 298 to Cys mutant, *Biochemistry 43*, 15230−45.
65. Bond, C. J., Jurica, M. S., Mesecar, A., and Stoddard, B. L. (2000) Determinants of allosteric activation of yeast pyruvate kinase and identification of novel effectors using computational screening, *Biochemistry 39*, 15333−43.

66. Ikeda, Y., Taniguchi, N., and Noguchi, T. (2000) Dominant negative role of the glutamic acid residue conserved in the pyruvate kinase M(1) isozyme in the heterotropic allosteric effect involving fructose-1,6-bisphosphate, *J. Biol. Chem. 275*, 9150−6.
67. Bollenbach, T. J., and Nowak, T. (2001) Kinetic linked-function analysis of the multiligand interactions on Mg(2+)-activated yeast pyruvate kinase, *Biochemistry 40*, 13097−106.
68. Mesecar, A. D., and Nowak, T. (1997) Metal-ion-mediated allosteric triggering of yeast pyruvate kinase. 1. A multidimensional kinetic linked-function analysis, *Biochemistry 36*, 6792−802.
69. Mesecar, A. D., and Nowak, T. (1997) Metal-ion-mediated allosteric triggering of yeast pyruvate kinase. 2. A multidimensional thermodynamic linked-function analysis, *Biochemistry 36*, 6803−13.
70. Nowak, T., and Suelter, C. (1981) Pyruvate kinase: activation by and catalytic role of the monovalent and divalent cations, *Mol. Cell. Biochem. 35*, 65−75.
71. Mattos, C., and Ringe, D. (1996) Locating and characterizing binding sites on proteins, *Nat. Biotechnol. 14*, 595−9.
72. Safo, M. K., Moure, C. M., Burnett, J. C., Joshi, G. S., and Abraham, D. J. (2001) High-resolution crystal structure of deoxy hemoglobin complexed with a potent allosteric effector, *Protein Sci. 10*, 951−7.
73. Ashizawa, K., McPhie, P., Lin, K. H., and Cheng, S. Y. (1991) An in vitro novel mechanism of regulating the activity of pyruvate kinase M2 by thyroid hormone and fructose 1, 6-bisphosphate, *Biochemistry 30*, 7105−11.

BI0474923